

3

The Accelerator Test Facility (ATF) and ATF2 at KEK

Future linear colliders such as ILC and CLIC require focusing the beams to nanometre sizes at the interaction point (IP) in order to reach the desired luminosity. The challenge of colliding nanometre sized beams at the IP involves three distinct issues: creating small emittance beams; preserving emittance during acceleration and transport; and focusing the beams to nanometre sizes before colliding them [46]. The ATF and ATF2 test facilities at KEK were built with the purpose of studying these issues experimentally.

In this Chapter, an overview of ATF and ATF2 projects is given, followed by detailed descriptions of the instruments for beam diagnostics at ATF2 with emphasis on the Interaction Point Beam Size Monitor (IPBSM). The issues of beam halo and study of Compton scattered electrons at ATF2 are presented in the last section.

3.1 Overview of ATF and ATF2 Projects

The ATF facility is a prototype DR to create small emittance beams as required for ILC. The ATF DR is a ~ 140 m circumference electron ring fed by an s-band linear accelerator which is used to accelerate the electron bunches produced by an RF gun to 1.3 GeV. In the normal ATF2 mode of operation, the DR delivers bunches of electrons with a 1.6 nC charge at 3.12 Hz to the extraction system. The typically measured (corrected) horizontal and vertical emittances are 2 nm-rad and 12 pm-rad respectively,

3. THE ACCELERATOR TEST FACILITY (ATF) AND ATF2 AT KEK

which means that it has succeeded in obtaining the emittances required for the ILC (see Fig.2.6).

The ATF2 facility, which was constructed in 2008, is a prototype of the final focus system for the future linear colliders (ILC and CLIC). It uses the beam extracted from the ATF DR to perform the nanometre beam size focusing and stabilisation with local chromaticity correction. The schematic layout of ATF and ATF2 facilities is shown in Fig.3.1. It can be seen that ATF2 is a new extraction (EXT) beam line of the ATF DR, many of the beam diagnostic instruments (eg. wire scanners) were moved from the old EXT to the ATF2 beam line.

3.1.1 ATF2 beam line

ATF2 is a follow-up to the Final Focus Test Beam (FFTB) experiment at SLAC, but with a different beam-line optics, shorter design based on local chromaticity correction, which results in a larger energy bandwidth.

The ATF2 beam line consists 7 dipoles, 3 septa, 49 quadrupoles, 5 sextupoles, 4 skew-sextupoles and 25 corrector magnets (see Fig.3.1 (upper)). The total length of the ATF2 beam line is ~ 90 m, with 52 m long EXT line and 38 m long final focus (FF) line.

The EXT line is used for the extraction and manipulation of the beam out of the DR and preparing it for injection into the FF. In the EXT line, the beam parameters can be measured with YAG screen monitor, wire scanners, Optical Transition Radiation monitors (OTRs) and different types of beam position monitors (BPMs). Besides, mismatch of the dispersion and betatron optical functions and betatron coupling, can be corrected with a set of dedicated upright and skew quadrupole magnets.

The optics of the ATF2 FF is a scaled-down version of the ILC design. The main design parameters of ATF2 are shown in Table 3.1 and compared with ILC. The comparison of the ATF2 and ILC BDS optics is shown in Fig.3.2.

The ATF2 beam line is normally operated with a 10 times larger horizontal IP β -function optics than originally designed to reduce the effect of multipole field errors to a level comparable to the tolerances of the ILC final focus design [48]. This optics is referred to as the “10BX1BY” optics because of the 10 times larger β_x^* and the same β_y^* compared with the original design, while the original optics is labeled as “1BX1BY”

3.1 Overview of ATF and ATF2 Projects

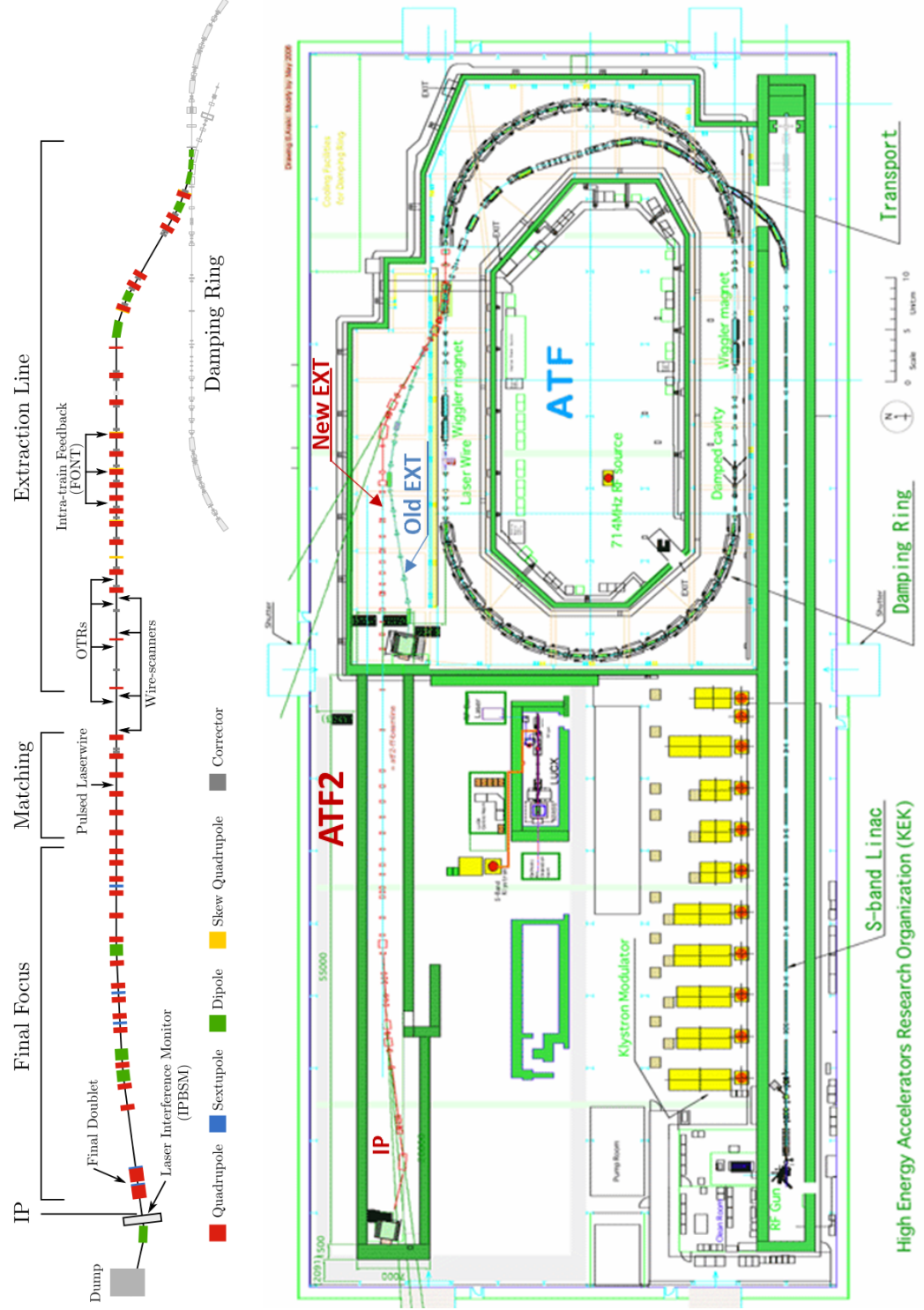


Figure 3.1: Schematic layout of the ATF and ATF2 facility: components of the ATF2 beam line are shown on the top of the scheme [47].

3. THE ACCELERATOR TEST FACILITY (ATF) AND ATF2 AT KEK

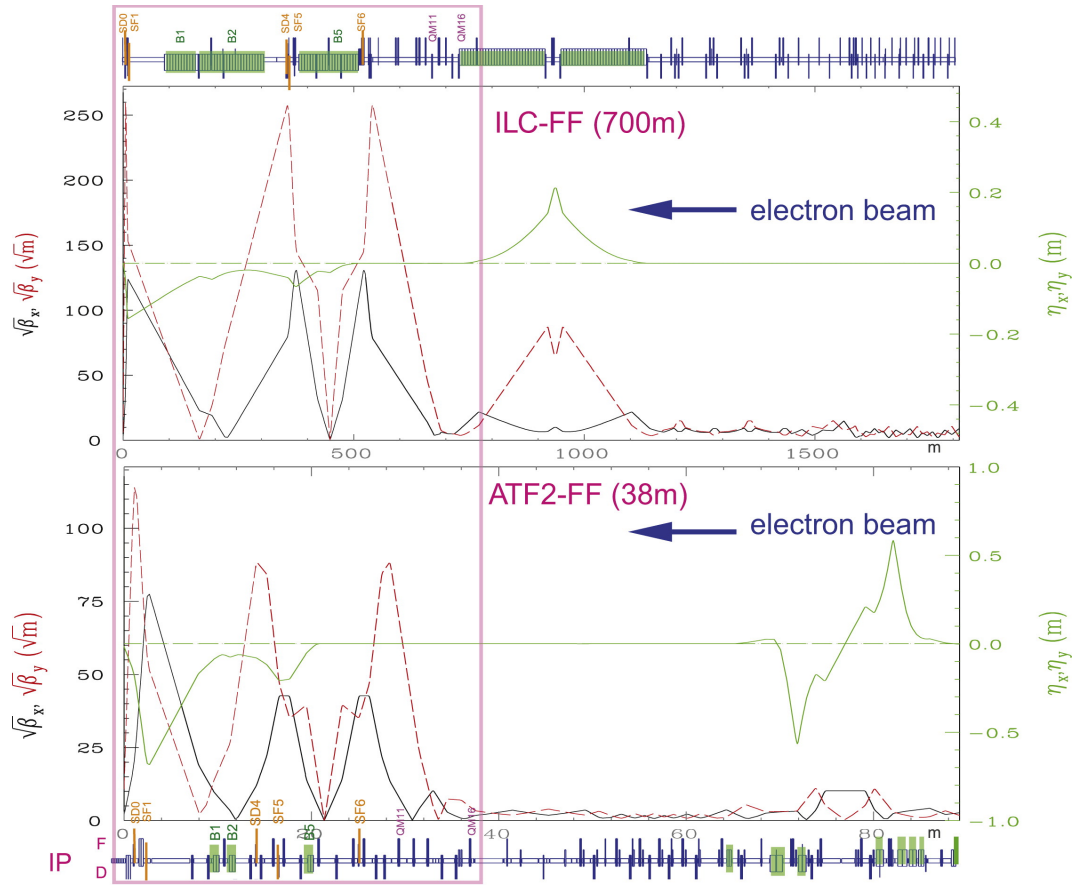


Figure 3.2: Comparison of ILC and ATF2 optics[45]

	ATF2	ILC
Beam energy [GeV]	1.3	250
β_y^* [mm]	0.1	0.48
ϵ_y [pm·rad]	12	0.07
σ_y^* [nm]	37	5.9
l^* (SiD/ILD detector) [m]	1.0	3.5/4.5
Energy spread (e^+/e^-) [%]	0.06~0.08	0.07/0.12
Chromaticity l^*/β_y^* (SiD/ILD detector)	10000	7300/9400

Table 3.1: Design parameters of ATF2 and ILC Final Focus [8] [10]

optics. Small (“10BX0.5BY”) and large (“100BX1000BY”) β -function optics are also used at times for different studies.

3.2 Goals of ATF2

The two main goals of ATF2 are:

- **Goal 1 - Achievement of small (37 nm) beam size:** demonstration of final focus system based on local chromaticity correction;
- **Goal 2 - Control of beam position:** demonstration of beam orbit stabilization with nano-meter precision at the IP, using intra-pulse feedback.

In addition to the main goals, other studies including lower β_y^* for CLIC, ground motion, beam halo and collimation studies are also performed at ATF2, as well as R&D on instrumentation.

3.2.1 Status of Goal 1

The first beam test at ATF2 started in Dec. 2008 focusing on the Goal 1. The history of minimum measured vertical beam size (σ_y) starting from Dec. 2010 to Jun. 2014 is shown in Fig. 3.3 (left). The beam size measurements are performed using a nanometer beam size monitor called “Shintake monitor” at the IP (see Section 3.4). The minimum measured beam size has decreased by a factor ~ 6 from ~ 300 nm in Dec. 2010 to ~ 44 nm in Jun. 2014. This achievement results from a number of different improvements, including the mitigation of higher order magnetic field errors and wakefield, suppression

3. THE ACCELERATOR TEST FACILITY (ATF) AND ATF2 AT KEK

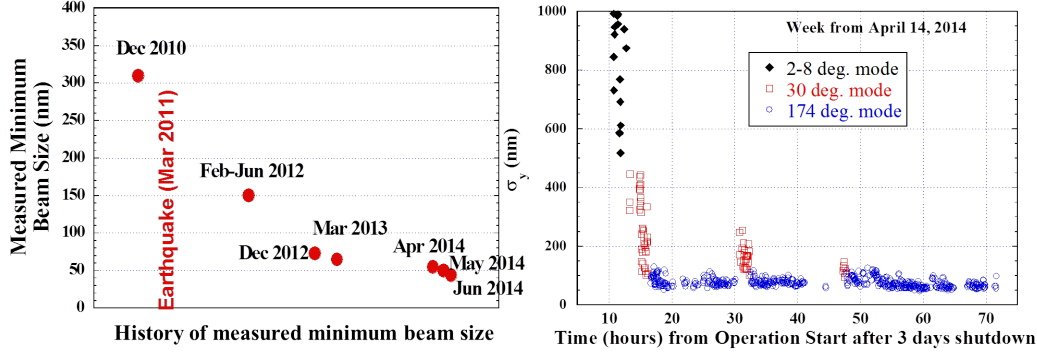


Figure 3.3: History of measured minimum beam size (left) and efficient beam tuning time after 3 days shutdown (right) [41]

of orbit drifts and jitter in the FF, improvement of the Shintake monitor etc.. Both hardware and software upgrades have contributed to these improvements [49, 41].

The minimum beam size of ~ 44 nm has been achieved repeatedly, but only at a beam intensity ten times lower than nominal (~ 0.16 nC)¹. An example from Jun. 2014, based on 10 consecutive measurements, is shown in Fig. 3.5. Even though this beam size (~ 44 nm) is still larger than the nominal 37 nm beam size, it has demonstrated the feasibility of doing a local chromaticity correction. Without chromatic correction the beam size would be ~ 450 nm. Further studies on beam jitter, wakefields and the stability of the Shintake monitor are on going to further reduce the beam size. Meanwhile, studies on wakefields are also carried out to understand the intensity dependence.

Another remarkable achievement of ATF2 is the efficient beam tuning after shutdown. Since the ILC detector will be operated in a “push-pull” mode², it is of great importance to recover the beam quickly after the short shutdowns needed to move the detectors in and out.

Fig. 3.3 (right) shows an example of the beam tuning time after 3 days shutdown. It can be seen that the beam can be squeezed from a few μm to ~ 60 nm in ~ 16 hours from the start of operation, while IP beam size tuning to a less than 60 nm beam only takes ~ 8 hours. These results imply that the small beam size, consequently the luminosity, can be quickly recovered after each “push-pull”.

¹At larger intensities, the minimum beam size rapidly gets larger.

²Switching between two detectors to allow operation of both at one single interaction region

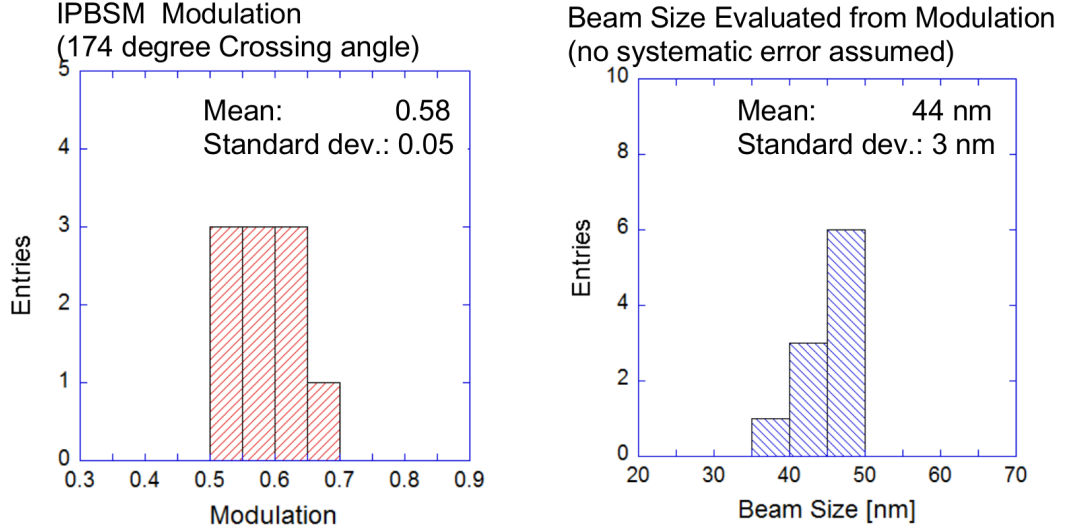


Figure 3.4: Example of consecutive beam size measurements: maximum measured modulation (left) and their corresponding minimum measured beam size (right) from 10 consecutive measurements performed on 12th June 2014 [13].

3.2.2 Status of Goal 2

The Goal 2 of ATF2 is to demonstrate the stabilization of the beam train trajectory at the nanometer level at the IP using an ILC-like multi-bunch train structure. In order to achieve this, a Feedback On Nanosecond Timescales (FONT) system [50] was developed and used in the extraction line beam diagnostic region to demonstrate a nm precision intra-pulse orbit feedback. This feedback system operates in 2 bunch mode with ILC-like bunch spacing (up to ~ 300 ns), it measures the position of the first bunch and then corrects the path of the second bunch. Sub-micron to micron level stability has been achieved [51, 52]. Further improvements of its performance is currently limited by the BPM resolution and bunch to bunch uncorrelated jitters.

At the IP region, special high resolution IP Beam Position Monitors (IPBPMs) [53] were installed in 2013 and 2014. This system uses a triplet (A,B and C) of BPMs based on low-Q and short gap cavities. The first block consists of two cavities (BPM A and B) installed upstream of the IP and the second block consists of single cavity (BPM C) installed downstream of the IP. Lateral and vertical adjustments can be applied in the range of 230-300 μm using 8 piezo-movers. The specified resolution of these BPMs is 1-2 nm and the presently achieved resolution is less than 50 nm with a beam intensity

3. THE ACCELERATOR TEST FACILITY (ATF) AND ATF2 AT KEK

of $0.4 - 0.5 \times 10^{10}$ [54, 55]. Commissioning and performance studies are ongoing for this system.

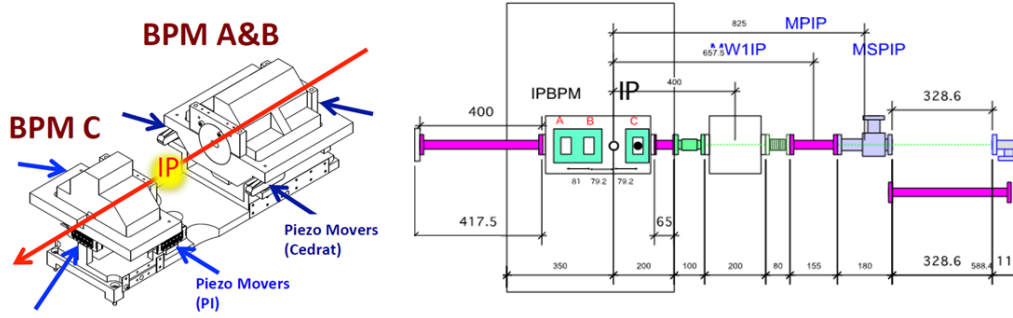


Figure 3.5: Schematic layout of IPBPM installed around the IP.

3.3 Instruments for beam diagnostic at ATF2

3.3.1 YAG:Ce screen monitors

Screen monitors are commonly used for the control of beam size and position. It is a destructive but direct and simple way of beam monitoring. When the screen is inserted, the electron beam collides with the inserted screen, and the screen emits light by scintillation. The emitted light guided by a lens system is then collected by a CCD camera, where the image of the beam profile is observed.

At ATF2, a Cerium activated Yttrium Aluminium Garnet (YAG:Ce) screen was installed at the location of MS1X at 7.4 m away from the exit of the DR with the purpose of measuring the vertical beam size, beam tilt and the momentum spread at the exit of the DR [56]. The screen has 10 mm diameter and it is made of 50 μm thick single crystal of YAG:Ce. A CCD camera (IMPREX IGV-B0610M) is used for the image collection. The schematic layout of the system is shown in Fig. 3.6 (upper left).

The minimum measurable beam size of YAG:Ce screen is limited by the following effects [56]:

- **Blurring effect:** since the YAG:Ce screen has finite thickness, the light is emitted along the whole length of a particle path and at all the angles (see Fig. 3.6

3.3 Instruments for beam diagnostic at ATF2

(lower left)). A lens system with certain geometrical acceptance can be used to optimize the resolution by cutting the light emitted with large angle while keeping the amount of collected light. However, still over 20 % of the radiated light reflects from the back surface of the crystal with finite emission angles, which further decreases the optical resolution. As the blurring effect depends on the thickness of the screen, thinner screens are preferred for small beam size measurement.

- **Resolution of the lens:** the quality of the lens is usually defined by their ability to resolve detail. The resolution of the presently used lens at ATF2 is $4.3 \mu\text{m}$. With this resolution a minimum beam size of $7 \mu\text{m}$ has been measured [56].
- **Saturation of YAG emission:** when the beam intensity is too high, both the CCD camera and the YAG screen can get saturated. While the saturation of CCD camera can be easily avoided by adding optical filters, the saturation of YAG emission is more complicated and difficult to deal with [57]. The saturation level of YAG:Ce screen used at ATF2 is estimated to be $0.25 \text{ pC}/\mu\text{m}^2$.

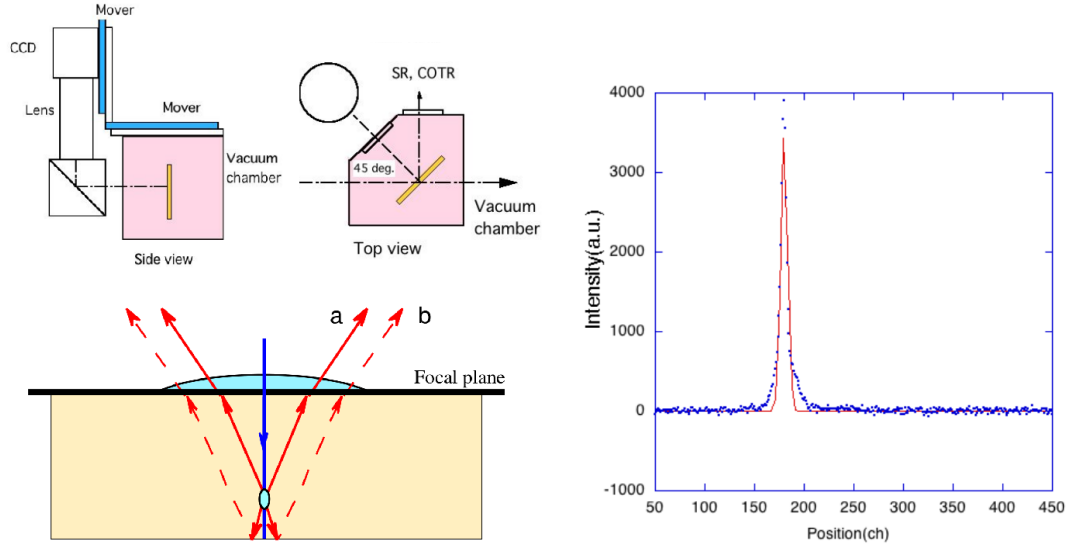


Figure 3.6: Upper left: schematic layout of the YAG:Ce screen system at ATF2, synchrotron radiation (SR) and coherent optical transition radiation (COTR) from the upstream are reflected to 90° ; Lower left: limitations on YAG optical resolution at large emission angles. Image from a point source is not sharp due to: finite crystal width and associated depth of focus problem (a) and light reflection from the back wall of a crystal (b) [58]; Right: an example of measured beam size using YAG:Ce screen [56]

3. THE ACCELERATOR TEST FACILITY (ATF) AND ATF2 AT KEK

With these constraints, the measured minimum vertical beam sizes at ATF2 using YAG:Ce screen was $7\text{ }\mu\text{m}$, while the minimum horizontal beam size was estimated to be $50\text{ }\mu\text{m}$ for the 45° injection as shown in Fig. 3.6 (upper left). One example of the measurement fitted to Gaussian distribution is shown in Fig. 3.6 (right). It can be seen that, the dynamic range of the measurement is $> 10^3$ in this case, and tails on the two side of the Gaussian distribution can be observed. These tails might be caused by the beam halo (if the blurring effect can be neglected).

3.3.2 Optical Transition Radiation system

The Optical Transition Radiation (OTR) monitor is based on the transition radiation effect. When intercepted by a thin metallic foil, the beam emits a light cone due to a pure classical electrodynamic process when a charged particle passes from one medium into another. In the vacuum in front of the foil, the particle has a certain electromagnetic field configuration, which is different from the field inside the medium, because the foil has a (complex) dielectric constant different from vacuum. By approaching the foil, the particles electro-magnetic field leads to a time-dependent polarization at the foil boundary. The change of this polarization emits the radiation, which combines coherently from different points at the foil to a characteristic intensity and angular distribution [59].

As shown in Fig. 3.7 the foil is inserted at certain angle to the beam (45° in most cases), the light is emitted in the forward direction as well as at 90° , because the metallic surface acts as a mirror. Depending on the particle energy, the angular distribution is peaked at the angle $\theta = 1/\gamma$ with γ the relativistic Lorentz factor. Typically 100 to 1000 beam particles yield 1 photon in the optical wavelength range. With appropriate optics, an image of the foil is recorded with a CCD camera.

At ATF2, four OTR monitors are installed in the diagnostic section in the EXT line, each of the OTRs uses a 1 cm diameter, $1\text{ }\mu\text{m}$ thick Al target foil (or Al coated kapton). This multi-OTR monitor system (mOTR) provides fast shot-by-shot measurements of beam profile, allowing fast reconstruction of the emittance and Twiss parameters [60, 61]. This system has been fully operational since Sept. 2011.

Comparing with the YAG screens, the OTRs can measure smaller beam size with a better resolution. The minimum measurable spot size is $\sim 2\text{ }\mu\text{m}$. The measurement resolution is of the order of a few percent of the measured spot size. Once the target

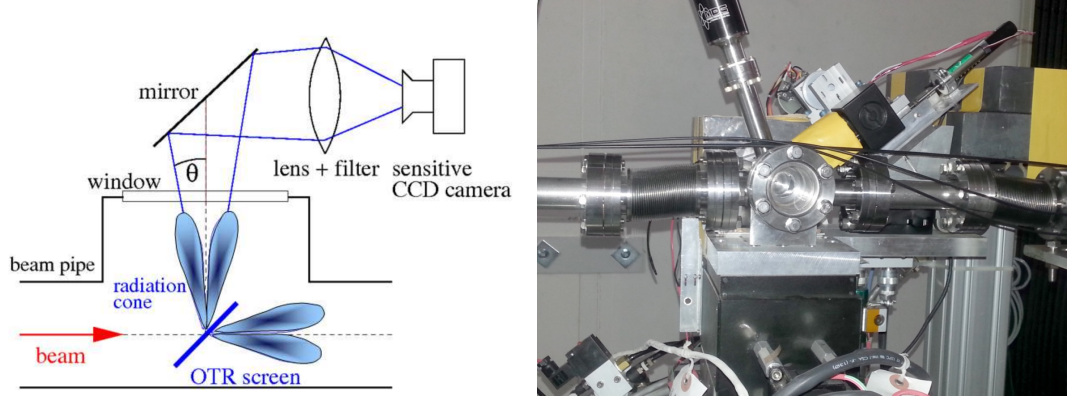


Figure 3.7: Schematic layout of an OTR screen measurement (left) [59] and the OTR system installed at ATF2 (right)

is inserted into the beam, the OTR measures the projected x and y spot sizes and the beam tilt (x - y correlation) on every pulse. This single-shot measurement is insensitive to beam position jitter, and is very fast. Full emittance measurements (x and y , plus coupling information), with statistical averaging can be made quickly [62].

The mOTR is being used routinely for beam size and emittance measurements at ATF2 and it plays an important role in the beam phase space and cross-plane coupling correction. However, effects of the OTR monitor chamber on the IP vertical beam size were found in June 2014 due to the wakefield generated by the vertical asymmetric geometry of the chamber [63]. This effect is currently under investigation.

Another important issue with the mOTR for beam size measurements is the long beam tails observed during the measurement. The beam tails can effect the Gaussian fit of the beam core, consequently the measurement resolution of the system. Their origin is not yet understood, they may come from beam halo or from chromatic aberrations of the OTR optics itself [64].

3.3.3 Wire scanners

At the ATF, wire scanners (WS) have been used to measure the beam size at the diagnostic section, IP and post-IP region. The beam is scanned by the wire and the photons generated by bremsstrahlung are detected by the photon detectors, installed downstream after a bending magnet to enable separating from the beam, using photomultipliers (PMTs). A Tapered Beam Pipe (TBP) [65] with a radius of 8 mm was

3. THE ACCELERATOR TEST FACILITY (ATF) AND ATF2 AT KEK

installed between QD10BFF and QD10AFF magnets (see Fig. B.1 in Appendix B) at the downstream of the diagnostic section, where β_y is relatively large, to reduce the background at the IPBSM detectors without exciting the wakefield. Fig. 3.8 shows the location of the different WS and their detectors at ATF2 as well as the previous extraction line (old ATF EXT line). The distance of the WS to the entrance of the EXT line, the beam size and the phase advance at the positions where different WS are installed are listed in Table 3.2 and compared with the parameters at the TBP and IP. In 2013 there were 3 WS installed at ATF2: MW2X, MW3X and post-IP WS. In 2005, before the completion of ATF2 line, these wire scanners have been installed in the old extraction (EXT) line of ATF (see Fig. 3.1 and Fig. 3.8 (upper)) together with other two wire scanners. First beam halo measurements have been performed using these wire scanners in 2005, which will be described in more detail in Section 3.5. Similar measurements were done in 2013 at the ATF2 beamline, which will be presented in Chapter 5.

	Position (m)	σ_x (μm)	σ_y (μm)	$\mu_x/2\pi$	$\mu_y/2\pi$
MW2X	43.54	88.54	11.77	2.98	2.27
MW3X	48.09	145.53	6.99	3.09	2.37
TBP	61.39	269.37	297.07	4.04	2.96
IP	89.30	8.93	0.03469	5.29	4.21
Post-IP WS	89.92	140.47	215.48	5.53	4.46

Table 3.2: Beam parameters ($10\beta_x^* \times 1\beta_y^*$)

Fig. 3.9 shows the structure of the WS. The total length of the WS is around 150 mm and the distance between two wire centers is 10 mm. The wire scanners are installed with an angle of 45° to the beam line to enable a simultaneous scan in the two transverse axes [66] (horizontal and vertical). The X and Y wires are used for horizontal and vertical measurements, respectively. An example of such measurements is shown in Appendix A (Fig. A.1). The U wire, which is 45° to X and Y wire is used to measure the correlation between horizontal and vertical measurements. In addition, two 10 μm tungsten wires with $+10^\circ$ and -10° tilts from the X direction are used to measure the tilt angle of the beam profile. As the resolution of the beam size measurement depends on the wire diameter, three Y wires with different diameters (7 μm , 10 μm and 50 μm) were installed to measure different vertical beam sizes (σ_y). The effect of the wire

3.3 Instruments for beam diagnostic at ATF2

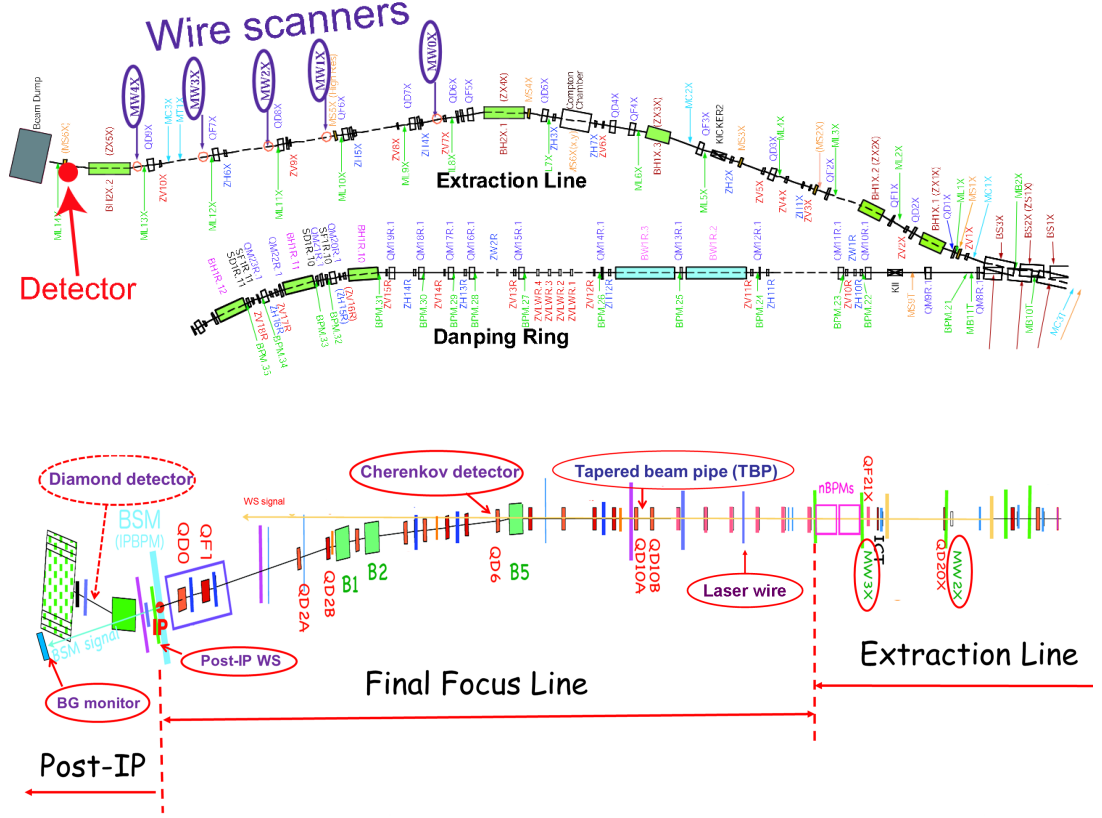


Figure 3.8: Location of wire scanners at the old ATF EXT line (upper) and at ATF2 (lower)

diameter on the beam size measurement can be taken into account by the following formula [67]:

$$\sigma_{true}^2 \approx \sigma_{measured}^2 - \left(\frac{d}{4}\right)^2 \quad (3.1)$$

where d is the wire diameter. This approximation is valid as long as the diameter is sufficiently small compared with the beam size. If the diameter is much larger than the beam size, the distribution of detected gamma rays might be different from a Gaussian distribution. The $7 \mu\text{m}$ wire can be used to measure beam sizes larger than $3.3 \mu\text{m}$ with an error less than 1%, while the $10 \mu\text{m}$ wire is used to measure beam size larger than $4.5 \mu\text{m}$ as shown in Ref. [67]. Near the IP, another carbon wire scanner (MWIP) with $5 \mu\text{m}$ thick wires is used as the first part of the IP beam size minimization procedure ($\sigma > 1 \mu\text{m}$).

3. THE ACCELERATOR TEST FACILITY (ATF) AND ATF2 AT KEK

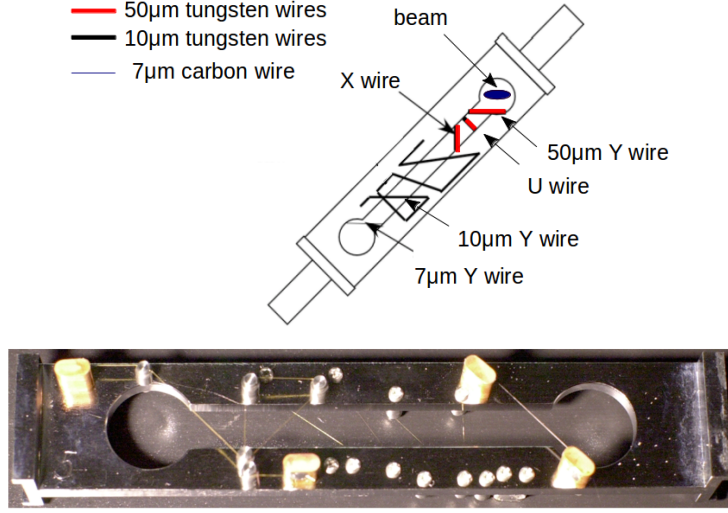


Figure 3.9: Structure of wire scanners at ATF2

3.3.4 Laser wire

Although wire scanners can be used to measure beam sizes of several μm , heat destruction can limit the performance of the carbon or tungsten wires especially for a high intensity beam [67]. Therefore, laser beams can be alternatives of the material wires for intense electron beams. Similar to wire scanners, laser wires can also be used for beam size measurement by measuring the photons generated by the inverse-Compton scattering between the laser and the electron beam.

Since the minimum observable electron beam size by a laser-wire is determined by the laser spot size, and the Compton scattering cross section is small, a high power pulsed laser source with strong laser focusing is required. A laser wire system with submicrometer resolution is installed in the “matching” region of the ATF2 beam line as shown in Fig. 3.8. This system uses a 150 mJ, 71 ps laser pulse with a wavelength of 532 nm. A minimum vertical beam size of $1.07 \pm 0.06(stat) \pm 0.05(sys) \mu\text{m}$ was measured using this system[68]. The laser wire system uses the same Cherenkov detector for Compton photon detection as used for the wire scanners in the EXT line [68, 69]. The schematic layout of the laser wire system is shown in Fig. 3.10.

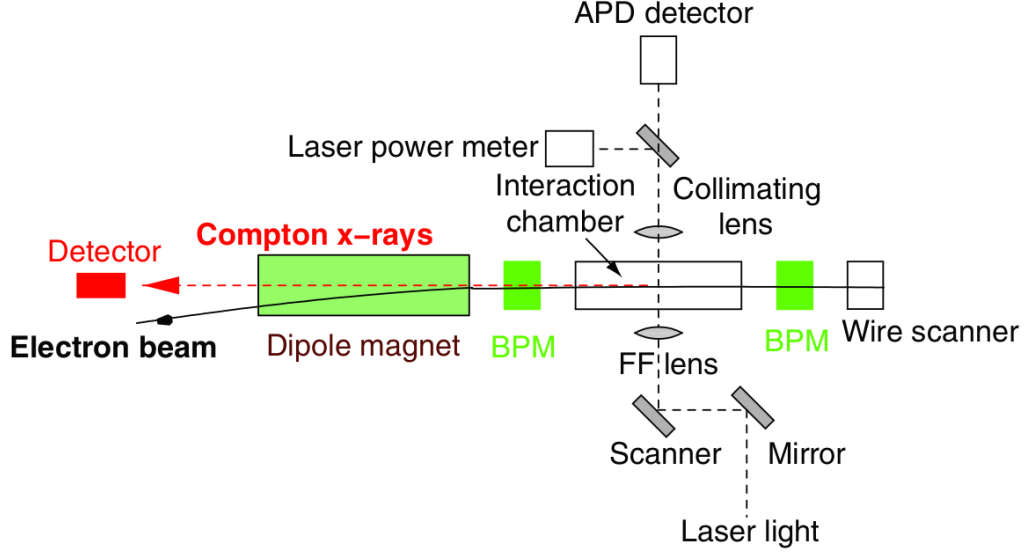


Figure 3.10: Schematic layout of the laser wire interaction region installation. The laser beam enters the interaction chamber from one side, interact with the beam and exit from the other side, where it is absorbed by the laser power meter. The APD detector is used for timing purposes [68, 69]

3.4 The Interaction Point Beam Size Monitor

At the IP of ATF2, as the designed vertical beam size is 37 nm, a speical beam size monitor is necessary for the tuning and for demonstrations of the focusing at nanometer level. For this purpose a so-called Shintake monitor (IP Beam Size Monitor (IPBSM)) is used. This monitor was invented by T. Shintake and first tested at the Final Focus Test Beam (FFTB) experiment at SLAC, where ~ 60 nm transverse beam sizes were successfully measured in the nineties [70].

The schematic layout of the IPBSM is shown in Fig. 3.11. A Nd:YAG Q-switch laser source is used to generate laser pulses of 532 nm wavelength. The laser beam is split into two: upper path and lower path. The two laser beams can be injected either separately to scan the beam, in the same way as the laser wire (laser wire mode), or they can be injected at the same time and intersect at the IP (IPBSM mode). In the latter case, the interference pattern formed by the two laser beams is then used to scan the beam.

Compton scattered photons are generated when the beam passes through the in-

3. THE ACCELERATOR TEST FACILITY (ATF) AND ATF2 AT KEK

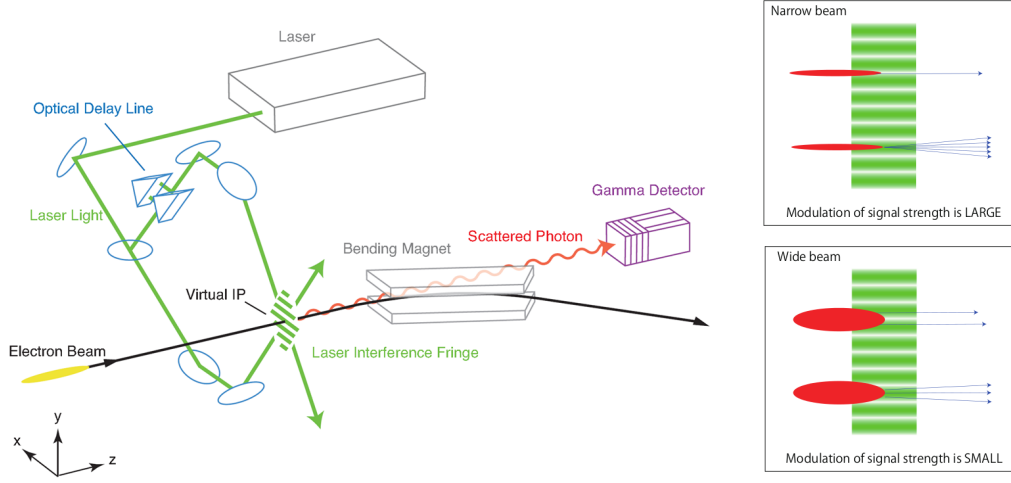


Figure 3.11: Shintake monitor for nanometer beam size measurement at the IP of ATF2

terference fringes. A CsI(Tl) calorimeter-type gamma detector (scintillator), installed 6.2 m downstream of the IP, is used for the Compton photon detection. In addition, another fast Cherenkov detector is under development for the 2 bunch operation, as the response of the CsI(Tl) scintillator is relatively slow to separate the signals from two subsequent bunches [71].

3.4.1 IPBSM mode

A well focused beam passes through the almost the same phase of the fringes, resulting in a large modulation in the photon signal, while a diluted beam passes through wider range of phases of the fringe pattern, leading to a small modulation. This behaviour is illustrated in Fig. 3.11. The modulation (M) of the Compton signal can be expressed as:

$$M = \frac{N_+ - N_-}{N_+ + N_-} \quad (3.2)$$

where N_+ and N_- are the maximum and minimum Compton signal intensities during a scan. For a Gaussian beam profile, the modulation can be expressed as a function of the laser crossing angle (θ) and electron beam spot size (σ):

$$M = |\cos\theta| \exp\left(-\frac{2\pi^2\sigma^2}{d^2}\right) \quad \text{with} \quad d = \frac{\lambda}{2\sin(\theta/2)} \quad (3.3)$$

where d is the interference fringe pitch i.e. the distance between adjacent peaks and $\lambda=532$ nm is the laser wave length.

3.4 The Interaction Point Beam Size Monitor

From Eq. 3.3 it can be seen that the beam size measurable range is determined by the interference fringe pitch and that the effective fringe pitch is defined by the laser crossing angle θ .

For the IPBSM mode, the crossing angle of the two laser beams can be mechanically switched among 174° , 30° and 2° to 8° (continuously adjustable). The measurable range for different crossing angles is shown in Table 3.3.

Crossing angle θ	174°	30°	8°	2°
Fringe pitch d	266 nm	$1.028 \mu\text{m}$	$3.81 \mu\text{m}$	$15.3 \mu\text{m}$
Measurable σ_y^*	20-100 nm	100-360 nm	360 nm - $1.4 \mu\text{m}$	1.4 - $6.0 \mu\text{m}$

Table 3.3: Measurable range of IPBSM at different modes [49].

An example of a vertical beam size measurement using the IPBSM is shown in Fig. 3.12. The Compton photon signal (G) is fitted using the following formula:

$$G(\theta) = G_0(1 - M \cos(\theta + \theta_0)) \quad (3.4)$$

from where a modulation of $M = 0.314$ is obtained. The phase between two successive maxima of 2π corresponds to 266 nm. The beam size extrapolated from M using Eq. 3.3 is 64.4 nm without any systematic error correction applied [47].

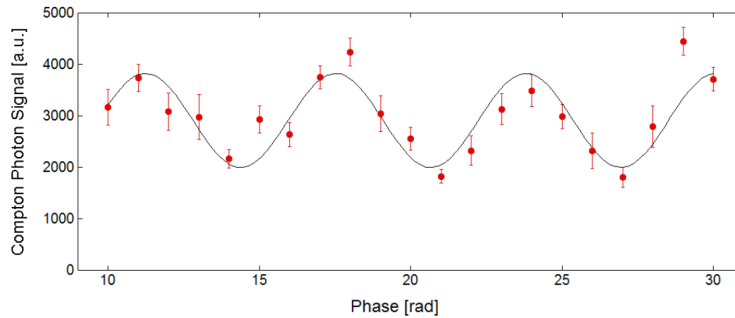


Figure 3.12: Example of a vertical beam size measurement using IPBSM (14th March 2013)

3.4.2 Laser wire mode

For the laser wire mode, the injection angle is usually set between 2° to 8° for σ_y measurement and 174° for σ_x measurement. However, since the laser spot size is typically

3. THE ACCELERATOR TEST FACILITY (ATF) AND ATF2 AT KEK

10-15 μm , which is comparable to the thickness of the carbon wires (5 μm), beam size measurement is usually performed using the MWIP wire scanner at the beginning of beam tuning. On the other hand, the laser wire mode is used to measure the laser spot size σ_{laser} and to finely align the laser position in the transverse plane after a preliminary alignment using screen monitor [49].

The nominal laser energy is 1.4 J/pulse. However, in order to improve the laser profile, the operating power is first reduced to 1.1 J/pulse. Then it is cut by 60% by a beam splitter on the laser table to prevent mirror damages. Besides, the laser transmission loss is estimated to be about 10%. Therefore, the final laser energy becomes ~ 0.4 J/pulse with two laser paths (IPBSM mode) and ~ 0.2 J/pulse for a single laser path (laser wire mode) [72].

3.4.3 Background sources for IPBSM

Backgrounds in the gamma detector are crucial to control for a good modulation resolution to be obtained. At ATF2, the background (BG) sources for the IPBSM are [18, 49]:

- Low energy (a few keV) photons generated by synchrotron radiation at the final doublet location, which can be stopped easily by the beam pipe aperture;
- Negligible amount of photons generated by the beam gas scattering;
- Slow neutrons from the dump in the end of the beamline, which can be separated from the signal in time by adjusting the detector's ADC timing gate;
- Bremsstrahlung photons generated by the beam halo hitting the final doublet magnets and the BDUPM bending magnet. These photons can have a high energy, up to the total energy of the electron beam (1.3 GeV).

Since the first three BG sources are either negligible or separable, the main BG remains the high energy bremsstrahlung photons generated by the beam halo, which can be controlled only by using dedicated collimators either for the beam halo itself or for the bremsstrahlung photons. At present, there is no dedicated collimator for beam halo at ATF2, background from the upstream is shielded by adjusting the vertical position of the TBP, installed in the high β_y location (see Fig. 3.8). Meanwhile, a

dedicated collimator system is being designed and will be installed in the EXT line for beam halo collimation [17].

For the bremsstrahlung photons collimation, three gamma collimators were installed in the post-IP region: a intermediate collimator inside the bending magnet, a fixed collimator and a movable collimator (see Fig. 3.13). This collimator system plays an important role in reducing the amount of BG photons and increasing the S/N ratio during fringe scans. However, since the bremsstrahlung BG photons generated at the FD propagate nearly parallel to the signal photons emitted at the IP, it is difficult to collimate a sufficient amount of BG while still maintaining signal acceptance. Thus bremsstrahlung photons remain a major source of BG in the detector. Although this can be partly mitigated by separating the signal from the BG in the analysis [49], further improvement of the performance of the IPBSM will require a good understanding and control of the beam halo.

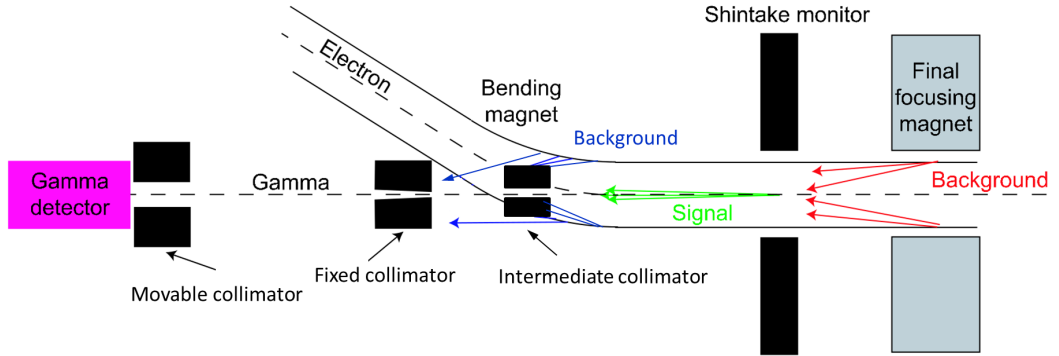


Figure 3.13: Schematic layout of the gamma collimators used for the control of BG photons[49]

3.5 Issues of beam halo at ATF2

As shown in the previous section, the nanometer beam size measurement using the IPBSM is very sensitive to background photons, the main source of which being photons generated by the beam halo hitting on the beam pipe. Thus, it is of great importance to understand the beam halo distribution and to find ways to control the background generated by the beam halo.

3. THE ACCELERATOR TEST FACILITY (ATF) AND ATF2 AT KEK

3.5.1 Beam halo in the damping ring

Beam halo consists of tails extending far beyond the Gaussian core of the beam. Although halo can be generated in many processes including beam-gas and thermal photon scattering, transverse wakefields, nonlinear fields in the magnets etc., the main source of transverse beam halo at ATF2 is expected from beam gas scattering while the longitudinal beam halo is dominated by the beam gas bremsstrahlung in the ATF damping ring [73].

Halo distributions due to several physical processes in ATF were estimated analytically based on the theory developed by K. Hirata and K. Yokoya [74]. Beam halo distributions due to beam-gas scattering, beam-gas bremsstrahlung and intra-beam scattering were studied and compared to data by D. Wang in Ref. [73]. The estimated beam halo transverse distribution due to beam gas scattering effect is shown in Fig. 3.14 with different vacuum pressures.

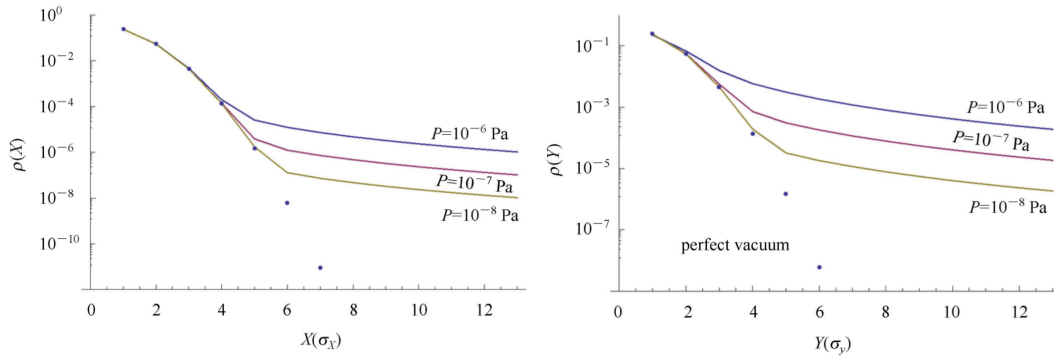


Figure 3.14: Horizontal(left) and vertical (right) beam distribution with different vacuum pressures (X and Y coordinate are normalized by RMS beam size) [73]

3.5.2 Beam halo measurement using wire scanners

First beam halo measurements were done in 2005 using the five WS located in the old EXT line of ATF, these measurements provide us with the first information about beam halo distribution in the EXT line [18]. In Fig. 3.15 we can see the beam core and beam halo distribution which were measured. Parametrizations for the horizontal and vertical distributions were proposed (see Fig. 3.15 bottom). These measurements have shown that the beam halo distribution depends on number of σ rather than absolute distance

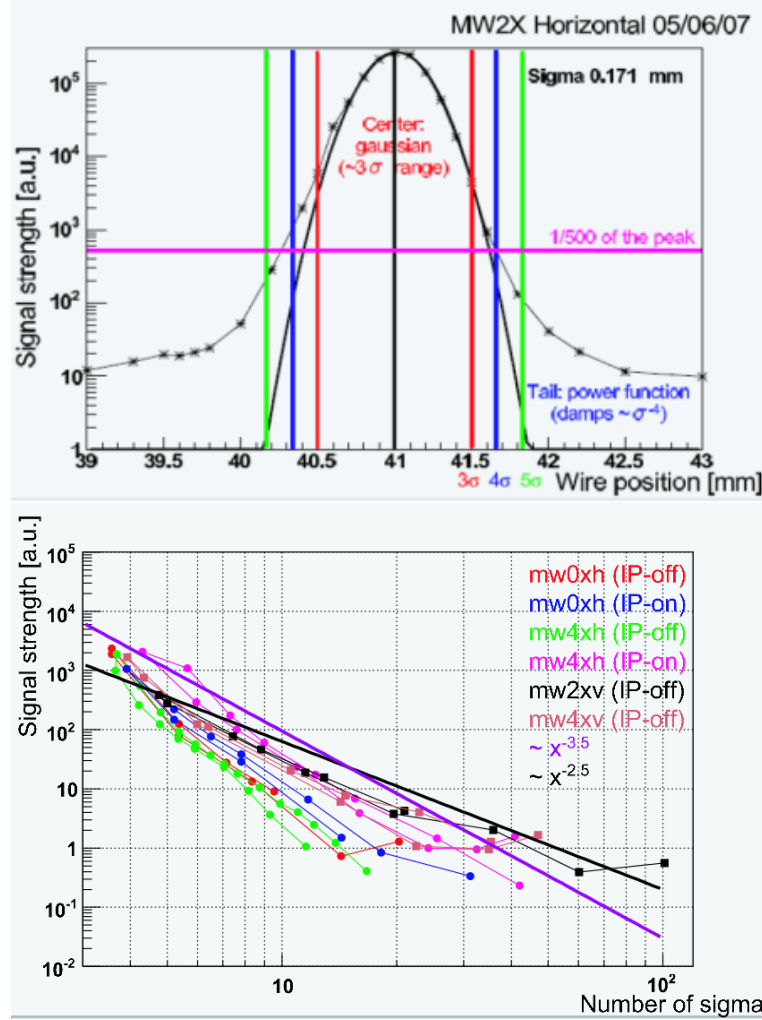


Figure 3.15: Top: Horizontal beam halo distribution measured with the MW2X WS in the old EXT line of ATF in 2005. Bottom: Measured beam halo distribution using different wire scanners for both vertical and horizontal directions as a function of number of sigmas. Vertical beam profiles are shown as squares and horizontal as circles and the difference of the Ion Pump (IP)-on data and the IP-off data is the vacuum level. For the IP-off data, some of the ion pumps in the ATF dumping ring were turned off to obtain data with degraded vacuum. The difference of the vacuum level is about 1:5.

from the beam center. Assuming a Gaussian distribution for the beam core (3σ) the parametrizations for the horizontal, ρ_H , and vertical, ρ_V , beam halo distribution are expressed as:

$$\rho_H = 2.2 \times 10^9 X^{-3.5} \quad (3.5)$$

3. THE ACCELERATOR TEST FACILITY (ATF) AND ATF2 AT KEK

$$\rho_V = \begin{cases} 2.2 \times 10^9 X^{-3.5} & \text{with } 3 < X < 6 \\ 3.7 \times 10^8 X^{-2.5} & \text{with } X > 6 \end{cases} \quad (3.6)$$

where X is the number of sigmas, and ρ_H and ρ_V are proportional to the number of particles, N , being $N = 10^{10}$ electrons in that case. In general, the distribution can be normalized to the number of particles and the resulting parametrization independent of N is:

$$\rho_H/N = 0.22 \times X^{-3.5} \quad (3.7)$$

$$\rho_V/N = \begin{cases} 0.22 \times X^{-3.5} & \text{with } 3 < X < 6 \\ 0.037 \times X^{-2.5} & \text{with } X > 6 \end{cases} \quad (3.8)$$

In 2013 the coefficients of the parametrization were recalculated taking the 4σ position as $1/500$ of the peak intensity ¹ (see Fig. 3.15) giving the following parametrization [75]:

$$\rho_H/N = 0.102 \times X^{-3.5} \quad (3.9)$$

$$\rho_V/N = \begin{cases} 0.102 \times X^{-3.5} & \text{with } 3 < X < 6 \\ 0.017 \times X^{-2.5} & \text{with } X > 6 \end{cases} \quad (3.10)$$

Since these parametrizations were obtained from the old EXT line and the present ATF2 EXT line differs from the old one, new measurements using the WS are required to verify the beam halo parametrization. Measurements using the MW2X and the post-IP WS installed at ATF2 were performed and are presented in Chapter 5. These measurements can also serve as references for the beam halo measurements using diamond sensors at the post-IP region.

3.5.3 Beam halo measurement using YAG:Ce screen

As the YAG:Ce screen was installed near the exit of DR, where the beam halo distribution is not affected by other effects during transport along the ATF2 beam line, it can provide important information on the beam halo generated in the DR. Therefore, beam halo measurement using YAG:Ce screen was proposed [76] and first measurements were carried out by T. Naito in 2014. In order to increase the measurement dynamic range, a 1 mm wide slit in the center of the screen is cut out in the vertical direction, so that the beam core can go through without any interaction (see Fig. 3.16).

¹In Suehara's parametrization, the ratio of the charge intensity between the central Gaussian and halo function is determined so that the density of the center is 500 times larger than the density at the 5σ position, however, from Fig. 3.15 it can be seen that the $1/500$ of the peak intensity corresponds to the 4σ position rather than 5σ position, especially on the right side of the plot.

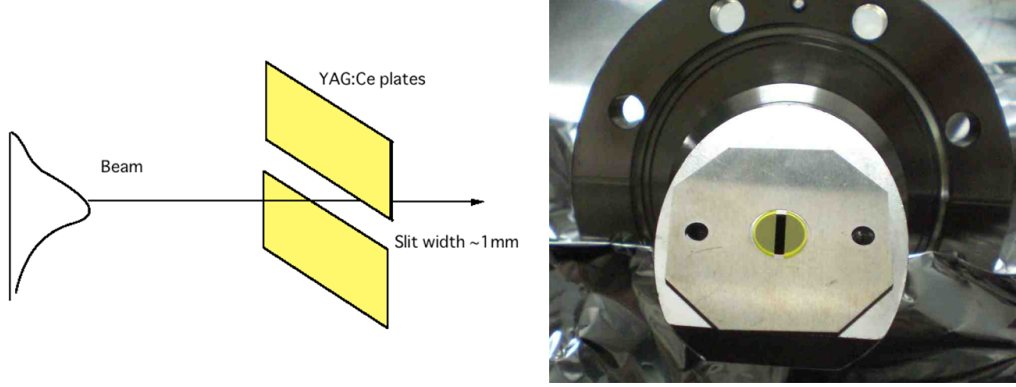


Figure 3.16: Beam halo measurement using YAG screen [77]

For the normalisation of beam halo, beam size measurement is required. However, at MS1X (7.4 m downstream of the exit of DR), where the YAG:Ce screen was initially installed for the energy spread measurement, there is no instrument (except for the YAG:Ce screen itself) for beam size measurement. Besides, the dispersion at MS1X location is relatively large (see Fig. C.1). Therefore, for the beam halo measurement, the YAG:Ce screen was moved in the summer of 2014 from the entrance of EXT line to the MW4X location. At the MW4X location the beam size can be measured by the OTRs or the wire scanners nearby.

The first measurement results were presented in Ref. [77] and shown in Fig. 3.17. The left plot shows the vertical distribution of the beam halo for a beam intensity of 0.15×10^{10} electrons. The red line shows the Gaussian distribution of a $20 \mu\text{m}$ vertical beam size. The beam halo exists over $200 \mu\text{m}$ ($10\sigma_y$) on both sides. The calibration of the core intensity is difficult due to saturation effects of the YAG:Ce screen. The right plot shows the intensity measurement of the beam core. The intensity is saturated even at the low intensity. The peak of the Gaussian distribution was estimated from the linear extrapolation. The dynamic range of the measurement is limited to $\sim 10^3$ due to the saturation effect as shown in Fig. 3.17 (right). Besides, the measured beam halo may be effected by the blurring effects as mentioned in 3.3.1. More measurements are planned in 2015 to investigate the beam halo distribution as a function of beam intensity and beam size. Further measurements can be done at the exit of the DR (at a dispersion free location) to compare the distribution with the simulated DR beam

3. THE ACCELERATOR TEST FACILITY (ATF) AND ATF2 AT KEK

halo distribution.

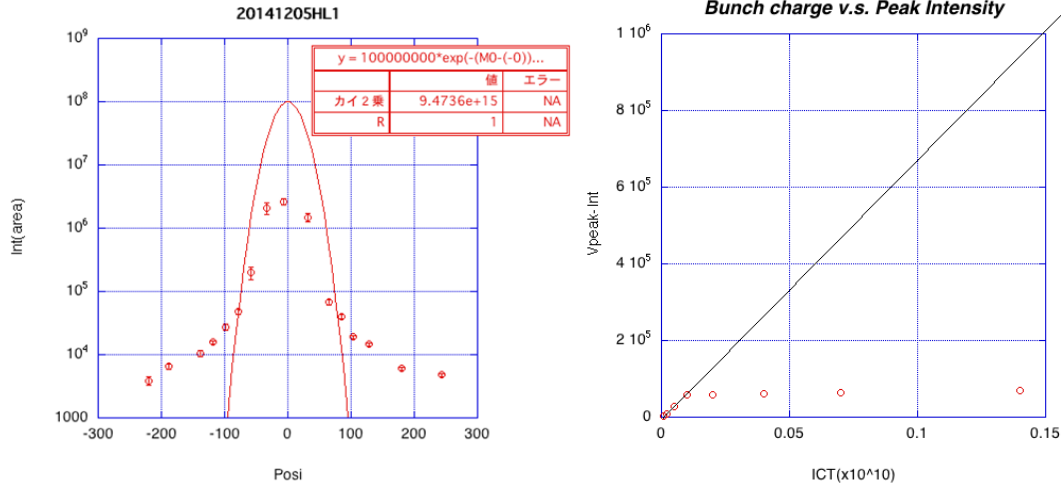


Figure 3.17: Beam halo measurement results using YAG:Ce screen [77]

3.6 Compton scattering and Compton recoil electrons

In Section 3.4 we mentioned that the Shintake monitor is based on the detection of the modulation of the signal from the Compton scattered photons. As the photons are separated from the electrons after the BDUMP bending magnet, it is possible to detect and study the spectrum of the Compton scattered electrons (Compton spectrum) after the bending magnet using the “in vacuum” DS.

3.6.1 Motivation for Compton spectrum measurement

The main purpose of measuring the Compton spectrum is to investigate the higher order contributions to the Compton process.

If we consider the Compton process as the interaction of an electron with a classical plane wave of frequency ω , then in the laser electric field (E), the maximum (transverse) velocity reached by an electron at rest $v_{max} = \frac{eE}{m}\omega \ll c$, the speed of light, an electron interacts with only one single photon (with the frequency ω) and radiates another photon [78]. Therefore, the electrons radiated intensity is a linear function of the intensity of the incident wave. This process can be expressed as:

$$e + \gamma \rightarrow e' + \gamma' \quad (3.11)$$

3.6 Compton scattering and Compton recoil electrons

However, in strong field, v_{max} approaches c , higher multipole radiation becomes significant, the electron can absorb multiple (n) photons from the laser field but radiates only a single photon. Therefore, the radiated intensity is no longer a linear function of the intensity of the incident wave. This process is called nonlinear Compton scattering and it can be expressed as:

$$e + n\gamma \rightarrow e' + \gamma' \quad (3.12)$$

A dimensionless parameter η was used to qualify the nonlinearity:

$$\eta = \frac{eE_{rms}}{m\omega} = \frac{e}{m} \sqrt{\frac{\rho_\omega}{\omega}} \quad (3.13)$$

where E_{rms} is the RMS electric field, m is the mass of the electron, ω and ρ_ω is the frequency and the number density of the laser photons. The nonlinear effects become significant only when η approaches or exceeds unity.

The nonlinear Compton scattering was observed in collision of 46.6 GeV and 49.1 GeV electrons of the Final Focus Test Beam (FFTB) at SLAC with $\eta \approx 0.4$ [79, 78]. The experimental set up for this experiment is shown in Fig. 3.18. In this experiment, a silicon-tungsten calorimeter (ECAL) was implemented for the Compton spectrum measurement. Nonlinear Compton scattering with the absorption of up to four laser photons in a single scattering event was observed in this measurement. At ATF2, with

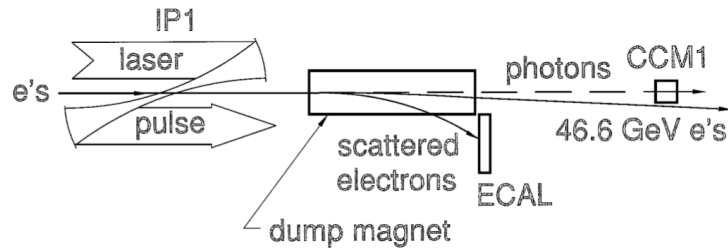


Figure 3.18: Schematic drawing of the Compton scattering experiment at FFTB [79]

an experimental set up similar to FFTB at the IP and post-IP region, it would be in principle possible to study the nonlinear Compton process and investigate its higher order contributions.

However, with the laser presently available, the factor η is calculated to be $\sim 7 \times 10^{-4}$ is $\ll 1$. For nonlinear Compton scattering detection, a high power laser is required.

3. THE ACCELERATOR TEST FACILITY (ATF) AND ATF2 AT KEK

This can be done by upgrading the laser system at ATF2 in the future. Calculated factors η for different laser settings can be found in Ref. [80].

As a preparation for future studies of nonlinear Compton scattering, detection of the first order Compton scattering spectrum using the “in vacuum” DS is planned. In the following sections, the Compton scattering process is explained in more detail and calculations for the expected Compton signal are presented based on the present laser configuration.

3.6.2 Compton scattering

Compton scattering is the inelastic scattering of a photon (with energy $h\nu \gtrsim m_e c^2$) by a charged particle (usually an electron). In this process, the incident photon with energy $h\nu$ and momentum $h\nu/c$ transfers part of its energy to the electron and is scattered with a decreased energy $h\nu'$ and momentum $h\nu'/c$. This was first discovered and measured by Arthur Compton in 1922[81].

Inverse Compton scattering

When an electron is not at rest, but colliding with a soft photon, the recoiling photon gains its energy by the transfer from the incoming electrons. This process is called inverse Compton scattering [82]. The difference between Compton scattering and inverse Compton scattering is shown in the schematics in Fig. 3.19. As the electrons at ATF2 are ultra-relativistic electrons, the Compton scattering in our experiment refers to the inverse Compton scattering.

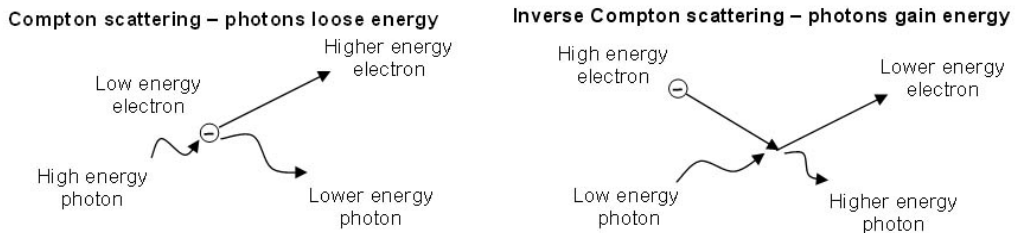


Figure 3.19: Compton scattering and inverse Compton scattering

3.6.3 Compton cross section and estimated rates

In the electron rest frame (denoted with *), the energy conservation and momentum conservation law is expressed as (see Fig. 3.20):

$$p_\gamma^* c + m_e c^2 = p_\gamma^{*'} c + \sqrt{p_e^{*'}^2 c^2 + m_e^2 c^4} \quad (3.14)$$

and

$$p_\gamma^* + p_e^* = p_\gamma^{*'} + p_e^{*'} \quad (3.15)$$

supposing the photon injected from +x direction (collision angle θ is considered as 0°) and the scattering angle for the photon is ϕ and for electron is ψ , then the 4-momentum can be written as:

$$\begin{aligned} p_\gamma^* &= \frac{E_\gamma^*}{c} \begin{pmatrix} c \\ 1 \\ 0 \\ 0 \end{pmatrix}, \quad p_e^* = \frac{m_e c^2}{c} \begin{pmatrix} c \\ 0 \\ 0 \\ 0 \end{pmatrix}, \\ p_\gamma^{*'} &= \frac{E_\gamma^{*'}}{c} \begin{pmatrix} c \\ \cos\phi^* \\ \sin\phi^* \\ 0 \end{pmatrix}, \quad p_e^{*'} = \frac{m_e c^2}{c} \begin{pmatrix} c \\ \cos\psi^* \\ \sin\psi^* \\ 0 \end{pmatrix} \end{aligned} \quad (3.16)$$

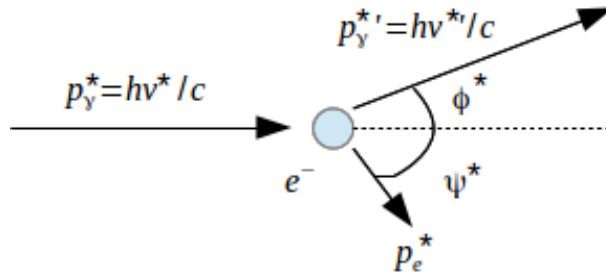


Figure 3.20: Compton scattering in the electron rest frame

The energy of the scattered photon ($E_\gamma^{*'}$) in the electron rest frame can be derived from 3.14 and 3.15 as:

$$E_\gamma^{*'} = \frac{E_\gamma^*}{1 + \frac{E_\gamma^*}{m_e c^2} (1 - \cos\phi^*)} \quad (3.17)$$

where E_γ is the initial energy of the photon, $m_e c^2 = 0.511$ MeV is the electron rest mass energy and ϕ is the scattering angle of the photon.

3. THE ACCELERATOR TEST FACILITY (ATF) AND ATF2 AT KEK

The differential cross section of photons scattered from a single free electron in lowest order of quantum electrodynamics can be expressed by the Klein-Nishina formula [83]:

$$\frac{d\sigma}{d\Omega} = \frac{r_e^2}{2} \left(\frac{E_{\gamma}^{*'}}{E_{\gamma}^*} \right)^2 \left(\frac{E_{\gamma}^{*'}}{E_{\gamma}^*} + \frac{E_{\gamma}^*}{E_{\gamma}^{*'}} - \sin^2 \phi^* \right) \quad (3.18)$$

and the total cross section can be expressed as a function of $x=2\frac{E_{\gamma}^*}{m_e c^2}$:

$$\sigma = 2\pi r_e^2 \frac{1}{x} \left(\left(1 - \frac{4}{x} - \frac{8}{x^2} \right) \log(1+x) + \frac{1}{2} + \frac{8}{x} - \frac{1}{2(1+x)^2} \right) \quad (3.19)$$

at lower frequencies ($\frac{h\nu}{m_e c^2} \ll 1$) this formula can be written as:

$$\sigma \approx \sigma_T \left(1 - x + \frac{13x^2}{10} + \dots \right) \quad (3.20)$$

and at higher frequencies ($\frac{h\nu}{m_e c^2} \gg 1$) it can be written as:

$$\sigma = \frac{3}{4} \sigma_T \frac{1}{x} \left(\ln(x) + \frac{1}{2} \right) \quad (3.21)$$

where

$$\sigma_T = \frac{8\pi}{3} r_e^2 = 6.65 \times 10^{-29} [m^2] \quad (3.22)$$

is the cross-section of Thomson scattering, which is considered as the low-energy limit of Compton scattering and represents the elastic scattering of a low energy photon by an electron at rest[84].

The parameters in the electron rest frame can be transformed to the parameters in the lab frame using the Lorentz transformation (see Fig. 3.21) [80, 85]:

$$E_{\gamma}^* = \gamma E_{\gamma} (1 - \beta \cos \phi^*) \quad \text{with} \quad \gamma = \sqrt{1 + \frac{E_e}{m_e c^2}} \quad (3.23)$$

$$\cos \phi^* = \frac{\cos \phi - \beta}{1 - \beta \cos \phi} \quad (3.24)$$

Inserting Eq. 3.23 and Eq. 3.24 into Eq. 3.17, the maximum ($\phi=0$) and minimum ($\phi = \pi$) energy of the scattered photon can be calculated to be ~ 29.5 MeV and ~ 1.17 eV, respectively [49].

At ATF2, the laser wavelength is $\lambda_l=532$ nm, therefore the single photon energy $E_{\gamma}=2\pi\hbar c/\lambda_l=2.33$ eV, the electron energy (E_e) is 1.3 GeV, the Lorentz factor $\gamma=2544$,

3.6 Compton scattering and Compton recoil electrons

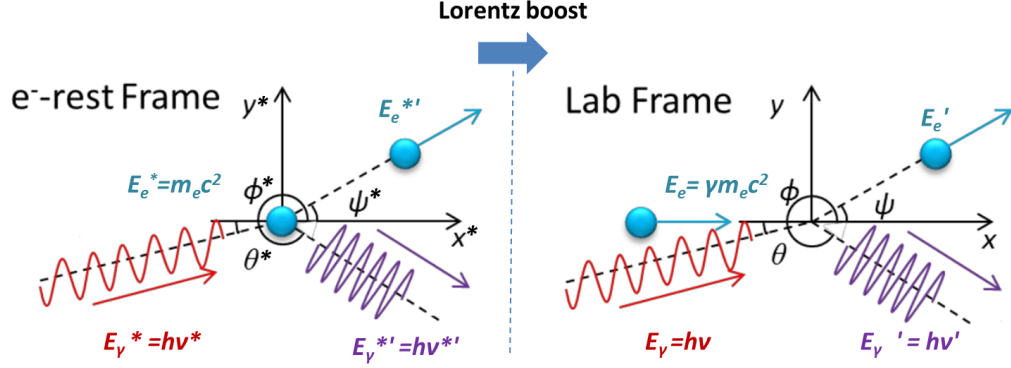


Figure 3.21: Lorentz transformation of Compton scattering from the electron rest frame to the Lab frame (modified from [85])

and therefore, the parameter x in Eq. 3.19 can be calculated to be $x = 2 \frac{\gamma E_\gamma}{m_e c^2} = 0.0116$ and the total cross section can be calculated according to Eq. 3.21 to be $\sigma = 0.65$ barn.

Knowing the total cross section, the number of scattered photons (N_γ) can be calculated as:

$$N_\gamma = L \cdot \sigma \quad (3.25)$$

where L is the luminosity for the Compton collision. Assuming the profile of the laser and electron beam to be Gaussian and that the two beams collide with an angle of θ and neglecting the divergence of the two beams, the luminosity can be expressed as [86]:

$$L = N_e N_l f \frac{\cos \frac{\theta}{2}}{2\pi} \frac{1}{\sqrt{\sigma_{ye}^2 + \sigma_{yl}^2} \sqrt{(\sigma_{xe}^2 + \sigma_{xl}^2) \cos^2 \frac{\theta}{2} + (\sigma_{ze}^2 + \sigma_{zl}^2) \sin^2 \frac{\theta}{2}}} \quad (3.26)$$

where N_e , N_l are the number of electrons in a bunch and the number of photons in a pulse, respectively, and f the number of collisions per unit time (Hz), θ is the collision angle, $\sigma_{x,y,ze}$ and $\sigma_{x,y,zl}$ are the three dimensional bunches r.m.s sizes for the electron beam (e) and for the laser beam (l).

The nominal laser and electron beam parameters at the IP of ATF2 are shown in Table 3.4.

Taken into account that the electron beam pulse (~ 27 ps) is much shorter than the laser pulse (3.4 ns) also $\sigma_{ye} \ll \sigma_{yl}$ and assuming a 90° collision angle, Eq. 3.26 can

3. THE ACCELERATOR TEST FACILITY (ATF) AND ATF2 AT KEK

Laser Beam		Electron Beam	
Single photon energy (E_γ)	2.33 eV	Energy (E_e)	1.3 GeV
Pulse energy (E_l)	0.2 J	Intensity (N_e)	10^{10}
Spot size ($\sigma_{x,yl}$)	15 μm	Vertical beam size (σ_{ye})	37 nm
RMS pulse width ($\frac{\sigma_{tl}}{c}$)	3.4 ns	Bunch length ($\frac{\sigma_{tl}}{c}$)	26.7 ps
Wave length (λ_l)	532 nm	Horizontal beam size (σ_{xe})	2.8 μm

Table 3.4: Laser and electron beam parameters at IP

be simplified to:

$$L = N_e N_l f \frac{1}{2\pi} \frac{1}{\sigma_{yl} \sigma_{xl}} \quad (3.27)$$

Combining Eq. 3.25 and Eq. 3.26 one can get the ratio of scattered photons to the total number of electrons per unit time as:

$$\frac{N_\gamma}{N_e} \frac{1}{f} = N_l \frac{1}{2\pi} \frac{1}{\sigma_{yl} \sigma_{xl}} \sigma = \frac{E_l}{E_\gamma} \frac{1}{2\pi} \frac{1}{\sigma_{yl} \sigma_{tl}} \sigma = 3.622 \times 10^{-7} \quad (3.28)$$

From Eq. 3.28 it can be seen that the value highly depends on the laser settings, with higher laser power and smaller laser beam size, a higher rate of scattered photons can be obtained. The calculated value of 3.622×10^{-7} is based on the present laser beam parameters shown in Table 3.4.

As the number of Compton recoil electrons¹ equals the number of scattered photons, assuming a total number of electrons of 10^{10} , the expected number of Comptons should be 3.622×10^3 , which is 7 order of magnitude less than the total beam. This level of signal is quite small comparing with the signal from beam halo, the total number of which is estimated to be in the order of 10^{-3} of the total beam [18] and it may cover the Comptons. However, since the Comptons differ from the beam halo in energies², it may be possible to sperate them using the BDUMP bending magnet installed after the IP. Nevertheless, as the beam halo distribution after the IP is unknown, prior to the detection of Comptons, measurement of beam halo distribution is essential. Besides, the beam core measurement is also required for the calibration of the beam halo and Comptons distribution. Thus, a total dynamic range of 10^7 is required for an instrument with capability of doing self-calibration.

¹For simplicity, the Compton recoil electrons are called Comptons from now on.

²The energies of Comptons are in principle more degreded than the beam halo.

3.6.4 Diamond sensor

In order to cover the large dynamic range required by detection of the Comptons, instead of using ECAL as detector for Comptons as the experiments done at FFTB(see Fig. 3.18), utilisation of diamond sensors (DS) was proposed for the detection of Compton signal at ATF2. Detailed description of the advantages of using DS are described in Chapter 6.

The schematic layout of using a diamond sensor for beam halo and Compton spectrum measurements is shown in Fig. 3.22. The DS is installed after the BDUMP bending magnet. The Comptons have less energy than the beam, thus they are deflected more than the beam and can be separated.

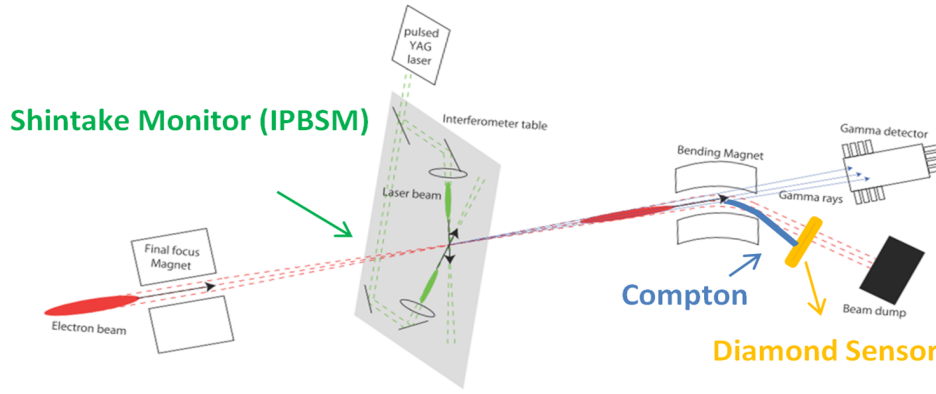


Figure 3.22: Schematic layout of using diamond sensor for beam halo and Compton spectrum measurements after the BDUMP bending magnet

Studies of the separation of the beam and Compton spectra, and of the optimal location of the DS are performed in Ref. [80] and Ref. [87]. The schematic layout of the deflection of electrons with different energies by the bending magnet is shown in Fig. 3.23. The angle of the bending magnet $\theta=20^\circ$ (see Fig. B.2). If the beam energy is $E_0=1.3$ GeV then the electrons with energy $E_0 - \Delta E$ are deflected with an angle of $\theta + \Delta\theta$ which results in horizontal displacements of Δx_0 and Δx at the exits of the bending magnet and the DS location, respectively. The displacement of the low energy electrons at the DS location can be calculated as:

$$\Delta x = \left(R \cdot \frac{1 - \cos\theta}{\cos\theta} + d \cdot \tan\theta \right) \frac{\Delta E}{E} \quad (3.29)$$

3. THE ACCELERATOR TEST FACILITY (ATF) AND ATF2 AT KEK

where $R=3883.25$ mm is the radius of the bending magnet, d is the distance from the exit of the bending magnet to the DS and $\frac{\Delta E}{E}$ is the energy spread. For the Comptons, since the maximum energy loss of the Comptons was calculated to be ~ 29.5 MeV, the maximum energy spread is $\frac{\Delta E_{max}}{E}=2.27\%$.

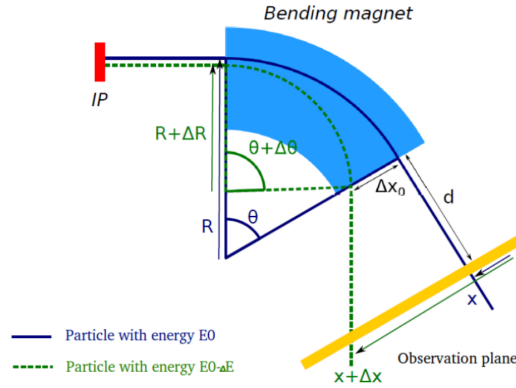


Figure 3.23: Schematic for diamond sensor location calculation [80]

Besides the uncertainty in displacement of the electrons due to their energy spread, the horizontal angular divergence (σ_{θ_x}) of the beam and beam halo can also be an important factor for the spectrum at the DS location. The spread of the beam (δ_{xb}) at the DS location due to angular divergence at the IP is given by:

$$\delta_{xb} = \sigma_{\theta_x}(l + d) \quad \text{with} \quad \sigma_{\theta_x} = \sqrt{\frac{\epsilon_x}{\beta_x}} \quad (3.30)$$

where $l=2.77$ m is the distance from IP to the exit of the bending magnet. For the beam with nominal parameters (1BX1BY optics) given in Table 3.2, the angular divergence σ_{θ_x} is calculated to be $\sigma_{\theta_x} = \sqrt{\frac{2 \times 10^{-9}}{4 \times 10^{-3}}} = 0.707$ mrad. However, the angular divergence of the beam halo can be N times larger than the beam. Therefore the spread of the halo (δ_{xh}) at the DS location can be expressed as:

$$\delta_{xh} = N \times \delta_{xb} \quad (3.31)$$

In order to detect the Comptons, the spectrum should not be dominated by angular divergence, therefore the following condition is required:

$$\Delta x > \delta_{xb,h} \quad (3.32)$$

3.6 Compton scattering and Compton recoil electrons

As the distance between exit of bending magnet and the end of beamline (DUMP) is limited ~ 2.5 m, and the DS should be kept at a certain distance to the DUMP to reduce the background from the backscattered particles from the DUMP, the horizontal DS location was chosen to be $d=1.35$ m. For the Comptons, with $d=1.35$ m and $\frac{\Delta E_{max}}{E}=2.27\%$, the calculated $\Delta x_{max}=16.8$ mm, while $\delta_{x_b}=2.91$ mm which is much smaller than Δx . However, for a beam halo with 10 times larger angular divergence of the beam ($N=10$), $\delta_{x_h}=29.1$ mm, which is larger than Δx_{max} .

Nevertheless, by increasing β_x , $\delta_{x_{b,h}}$ can be decreased. Therefore, during the experiments for Comptons detection, large β_x optics are preferred. First attempt of measuring Comptons spectrum were performed and described in Chapter 9.

3. THE ACCELERATOR TEST FACILITY (ATF) AND ATF2 AT KEK